bacteria. Two concentrations of dissolved Fe were added: iron-sufficient ([total Fe] = 8.41 μM, computed concentration of inorganic Fe(III), [Fe′] = 40 nM, although ferric hydroxides will precipitate at this concentration), and iron-deficient [total Fe] = 12.9 nM, [Fe′] = 25 pM). Quotas were measured using $^{55}FeCl_3$ (0.52 Ci mol^{-1}, DuPont) which was added as 1% and 100% of total Fe in the sufficient and deficient media, respectively[15]. Sodium ^{14}C-bicarbonate (5 Ci mol^{-1}, Dupont) was added at 1% of the final concentration to all dissolved media.

A marine bacterium, strain Ju188[10], isolated from the Sargasso Sea was used as a particulate source of Fe. Cultures were grown to stationary phase in 400 ml of Fe-sufficient AQUIL with 50 mg l^{-1} glucose, or in iron-deficient AQUIL with 100 mg l^{-1} glucose[10,11]. Iron was added as ^{55}Fe as described above. ^{14}C-glucose (3 Ci mol^{-1}, Amersham) was 1% of the final glucose concentration. To remove dissolved Fe, the bacteria were centrifuged, washed twice in Fe-free AQUIL with 100 μM EDTA and the final bacterial pellet was resuspended in Fe-free AQUIL. The mean quotas of the iron-rich and iron-poor bacterial prey were 101 ± 32 and 3.92 ± 1 μmol Fe per mol C, respectively.

Mixotrophs grown in these different media were harvested at late exponential phase, filtered onto 2-μm polycarbonate filters and rinsed with Ti(III)-citrate EDTA reagent to remove extracellular iron[25]. Bacteria trapped on these filters represented <1% of the total bacterial biomass. Bacterial abundance and particulate iron concentration in control flasks without flagellates did not change significantly during the experiments.

^{14}C and ^{55}Fe activity was measured by dual-label liquid scintillation counting. Iron quotas were measured in 3 separate experiments, each of which had between 2 and 4 replicates. Samples used for quota determinations were fixed simultaneously for biomass determinations by epifluorescence microscopy. Quotas for cells grown on bacteria were derived by dividing the amount of Fe:cell determined using radiotracers by the mean C:cell from image analysis.

Determination of *Ochromonas* C content. Photographs were taken of DAPI stained *Ochromonas* slide preparations using a camera mounted on a Leica epifluorescence microscope (400×). Photos were scanned and binarized to size the cells using UTHSCSA Image Tool version 1.27. At least 25 cells were sized per treatment. Standard error of estimated volumes was 5–8%. Cell carbon was estimated using a factor of 150 fg C μm^{-3} (ref. 26).

Cell C biomass estimates derived using image analysis (IA) were compared with those estimated using the ^{14}C incorporated by the mixotrophs and dividing by cell abundance in the dissolved treatments in order to verify the choice of the C conversion factor. Mean C estimates among methods were not significantly different (Fe-sufficient dissolved: IA = 1.26 ± 0.4 pmol C vs ^{14}C = 1.4 ± 0.22 pmol C, p = 0.26, and Fe-deficient dissolved: IA = 1.23 ± 0.27 pmol C vs ^{14}C = 1.21 ± 0.2 pmol C, p = 0.81).

Regeneration and gross-growth efficiencies. For dissolved activity (^{55}Fe), samples from the quota experiments were filtered though a 0.2-μm Acrodisc syringe-tip filter. Regeneration efficiencies were calculated from the total amount of Fe measured in the dissolved phase divided by the total amount of Fe ingested[11]. Gross Fe growth efficiencies were calculated by dividing the total ^{55}Fe activity in the mixotrophs at the end of a given time interval by the total ^{55}Fe activity ingested during the same interval, determined from the total number of bacteria grazed multiplied by the ^{55}Fe per bacterium (ref. 11). As we did not control for the possibility that regenerated Fe was reassimilated by *Ochromonas*, the Fe regeneration efficiencies and the gross Fe growth efficiencies should be regarded as maximum and minimum estimates, respectively. Carbon derived by heterotrophic growth was calculated by dividing the amount of bacterial C retained by *Ochromonas* when grazing on ^{14}C-labelled bacteria by the total amount of C per *Ochromonas* determined by image analysis. The ^{14}C contained in undigested bacteria (between 1 and 4 bacteria per cell) was subtracted from the total ^{14}C measured in the mixotrophs.

Received 24 November 1997; accepted 1 September 1998.

1. Johnson, K. S., Gordon, R. M. & Coale, K. H. What controls dissolved iron concentrations in the world ocean? *Mar. Chem.* **57,** 137–161 (1997).
2. Rich, H. W. & Morel, F. M. M. Availability of well-defined iron colloids to the marine diatom *Thalassiosira weissflogii*. *Limnol. Oceanogr.* **35,** 652–662 (1990).
3. Price, N. M. & Morel, F. M. M. in *Iron Transport and Storage in Microorganisms Plants and Animals: Metal Ions in Biological Systems* (eds Sigel, A. & Sigel, H.) 1–36 (Decker, New York, 1998).
4. Coale, K. H. *et al.* A massive phytoplankton bloom induced by an ecosystem-scale iron fertilisation experiment in the equatorial Pacific. *Nature* **383,** 495–501 (1996).
5. Hudson, R. J. M. & Morel, F. M. M. Iron transport in marine phytoplankton: Kinetics of cellular and medium control reactions. *Limnol. Oceanogr.* **35,** 1002–1020 (1990).
6. Maldonado, M. T. & Price, N. M. Utilization of iron bound to strong organic ligands by plankton communities in the subarctic Pacific Ocean. *Deep-Sea Res.* (in the press).
7. Rothhaupt, K. O. Utilization of substitutable carbon and phosphorus sources by the mixotrophic chrysophyte *Ochromonas* sp. *Ecology* **77,** 706–715 (1996).
8. Caron, D. A. *et al.* Light-dependent phagotrophy in the freshwater mixotrophic chrysophyte *Dinobyron cylindricum*. *Microb. Ecol.* **25,** 93–111 (1993).
9. Raven, J. A. Phagotrophy in phototrophs. *Limnol. Oceanogr.* **42,** 198–205 (1997).
10. Tortell, P. D., Maldonado, M. T. & Price, N. M. The role of heterotrophic bacteria in iron-limited ocean ecosystems. *Nature* **383,** 330–332 (1996).
11. Chase, Z. & Price, N. M. Metabolic consequences of Fe deficiency in heterotrophic marine protozoa. *Limnol. Oceanogr.* **42,** 1673–1684 (1997).
12. Hutchins, D. A., DiTullio, G. R. & Bruland, K. W. Iron and regenerated production—evidence for biological iron recycling in two marine environments. *Limnol. Oceanogr.* **38,** 1242–1255 (1993).
13. Sunda, W. G. & Huntsman, S. A. Iron uptake and growth limitation in oceanic and coastal phytoplankton. *Mar. Chem.* **50,** 189–206 (1995).
14. Raven, J. A. The iron and molybdenum use efficiencies of plant growth with different energy, carbon and nitrogen sources. *New Phytol.* **116,** 1–18 (1988).
15. Maldonado, M. T. & Price, N. M. Influence of N substrate on Fe requirements of marine centric diatoms. *Mar. Ecol. Prog. Ser.* **141,** 161–172 (1996).
16. Barbeau, K., Moffett, J. W., Caron, D. A., Croot, P. L. & Erdner, D. L. Role of protozoan grazing in relieving iron limitation of phytoplankton. *Nature* **380,** 61–64 (1996).
17. Twiss, M. R. & Campbell, P. G. C. Regeneration of trace metals from picoplankton by nanoflagellate grazing. *Limnol. Oceanogr.* **40,** 1418–1429 (1995).
18. Sanders, R. W. Mixotrophic protists in marine and freshwater ecosystems. *J. Protozool.* **38,** 76–81 (1991).
19. La Roche, J., Boyd, P. W., McKay, M. L. & Geider, R. J. Flavodoxin as an in situ marker for iron stress in phytoplankton. *Nature* **382,** 802–805 (1996).
20. Chavez, F. P., Buck, K. R., Service, S. K., Newton, J. & Barber, R. T. Phytoplankton variability in the central and eastern tropical Pacific. *Deep Sea Res. II* **43,** 835–870 (1996).
21. Strøm, S. & Welschmeyer, N. A. Pigment-specific rates of phytoplankton growth and microzooplankton grazing in the open subarctic Pacific Ocean. *Limnol. Oceanogr.* **36,** 50–63 (1991).
22. Constantinou, J. *Mixotrophic Nanoflagellates in Marine Microbial Food Webs.* Thesis, Univ. Hawaii (1994).
23. Stoecker, D. K., Gustason, D. E. & Verity, P. G. Micro- and mesoprotozooplankton at 140° W in the equatorial Pacific: heterotrophs and mixotrophs. *Aquat. Microb. Ecol.* **10,** 273–282 (1996).
24. Price, N. M. *et al.* Preparation and chemistry of the artificial algal culture media Aquil. *Biol. Oceanogr.* **6,** 443–462 (1988/89).
25. Hudson, R. J. M. & Morel, F. M. M. Distinguishing between extra- and intracellular iron in marine phytoplankton. *Limnol. Oceanogr.* **34,** 1113–1120 (1989).
26. Børsheim, K. Y. & Bratbak, G. Cell volume to cell carbon conversion factors for a bacterivorous *Monas* sp. enriched from seawater. *Mar. Ecol. Prog. Ser.* **36,** 171–175 (1987).
27. Peters, F. The prediction of planktonic protistan grazing rates. *Limnol. Oceanogr.* **39,** 195–205 (1994).
28. Bjørnsen, P. K. & Kuparinen, J. Growth and herbivory by heterotrophic dinoflagellates in the Southern Ocean, studied by mesocosm experiments. *Mar. Biol.* **109,** 397–405 (1991).
29. Barber, R. T. *et al.* Primary productivity and its regulation in the equatorial Pacific during and following the 1991–1992 El Niño. *Deep Sea Res. II* **43,** 933–969 (1996).
30. Binder, B. J., Chisholm, S. W., Olson, R. J., Frankel, S. L. & Worden, A. Z. Dynamics of picophytoplankton, ultraphytoplankton and bacteria in the central equatorial Pacific. *Deep-Sea Res. II* **43,** 907–931 (1996).
31. McCarthy, J. J., Garside, C., Nevins, J. L. & Barber, R. T. New production along the 140° W in the equatorial Pacific during and following an El Niño event. *Deep-Sea Res. II* **43,** 1065–1093 (1996).

Acknowledgements. We thank M. T. Maldonado and J. Granger for technical advice and comments on the manuscript, and D. M. Karl for discussion. Technical assistance was provided by P. Fenwick and A. Soucisse. R.M. was supported by a FCAR (Quebec) student scholarship. This work was funded by NSERC (Canada) grants to D.F.B. and N.M.P., and by the McGill Faculty of Graduate Studies and Research. This is a contribution to the Canadian JGOFS program and to the GRIL.

Correspondence and requests for materials should be addressed to N.M.P. (e-mail: nprice@bio1.lan.mcgill.ca).

Seismic evidence that the source of the Iceland hotspot lies at the core–mantle boundary

D. V. Helmberger, L. Wen & X. Ding

Seismological Laboratory 252-21, California Institute of Technology, Pasadena, California 91125, USA

Although Morgan[1] proposed in 1971 that hotspots such as Iceland were the result of hot, rising mantle plumes, it is still debated whether plumes originate from a thermal boundary just above the core–mantle boundary or at the base of the upper mantle[2]. Although seismic evidence of plumes in the upper mantle is accumulating[3], narrow plume conduits in the deep mantle have yet to be detected. Details of plume formation in the lower mantle have therefore remained largely unconstrained[4]. Here, however, we present seismic evidence for the presence of a localized patch of material with ultra-low seismic wave speed, located at the core–

mantle boundary beneath the Iceland hotspot, and propose that this zone represents the hot, partially molten source region of the Iceland mantle plume. Through the modelling of seismic waveforms, we constrain the seismic velocity structure at this patch of the core–mantle boundary using a numerical–analytical interfacing code[5] designed to reproduce the complex interference of shear-wave phases transmitted through, and refracted at, the boundary[6]. Although this structure is difficult to constrain precisely, our preferred model consists of a dome which is 250 km wide, 40 km high and contains P- and S-wave velocity (wavespeed) reductions of 10% and 30%, respectively.

Recent advances in seismological research have shown that the seismic phase SKS and associated P diffractions SPdKS and SKPdS are extremely useful for the study of structure at the base of the mantle. SPdKS and SKPdS differ from SKS by two short segments of P-wave paths at the base of the mantle, while their propagation paths in the upper and middle mantle are virtually identical[7] (Fig. 1). The complex waveform interference of these phases are strongly sensitive to P and S velocity structure at their core-entry and core-exit points[8]. Most observations of anomalous interference between SKS and SPdKS (or SKPdS) have been observed for core–mantle boundary (CMB) sampling regions which lie beneath the central Pacific where strongly varying P-wave velocity reductions of up to 10% have been found. These structures appear to be centred beneath a broad low-shear-velocity region of the lower mantle constrained by anomalously delayed S-SKS and SKS-SKKS differential travel times[9,10]. Normal SPdKS observations are found for regions sampled around the Pacific Ocean and can be modelled by standard seismic velocity models such as PREM[11,12]. These features can be seen in Fig. 2b, where SKS remains relatively simple out to 111° and the separation between SKKS and SKS is easily modelled by PREM-like models. This simplicity is in contrast to observations obtained at KEV and KRK from South American events (Fig. 2c). The enhanced P-diffractions can be produced by decreasing the P-velocity in a radially uniform model (1-D) which shifts the S-to-P critical angle to smaller distances at each CMB crossing[7,14] and produces the secondary pulse. These segments are indicated in map-view in Fig. 2a for great-circle paths. There is some evidence for broadening on the VAL and STU records (Fig. 2a) and an associated increase in SKKS-SKS differential timing separation indicative of lower velocities[11]; however, these CMB samples (Fig. 2a) are located considerably south of the KEV and KRK samples.

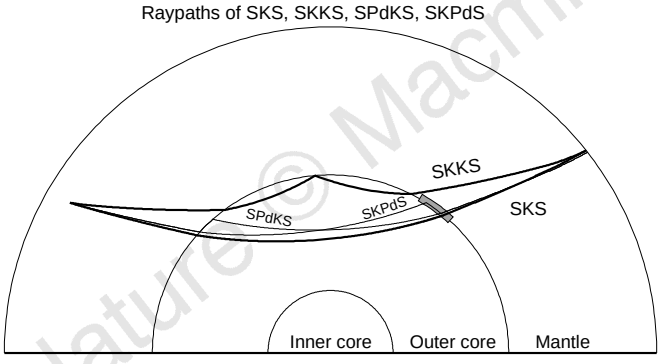

Figure 1 Ray-path geometry. Cross-section through the PREM (preliminary reference Earth model)[25] showing the ray-paths of SKS, SKKS and two diffracted phases SPdKS (source-side) and SKPdS (receiver-side) at a distance of 118°. The latter phases are caused by the critical angle S-to-P and P-to-S conversion at the CMB which produces P-wave diffractions along this boundary. PREM-like models, with constant velocities across D″ (the transition zone at the CMB), predict the bifurcation of SKS near 106° which leads to a long-period waveform interference near 112°, depending on the source duration. If the P-wave velocity is reduced, the interference shifts to shorter distances. Identifying this bifurcation point, therefore, becomes an excellent tool for fixing the P-wave velocity at a particular location on the CMB. We note that the only significant region sampled differentially by these paths occurs in the 1-D outer core and at the CMB. The paths through the crust and mantle are essentially identical[7]. This minimizes the uncertainties of waveform modelling due to crust and mantle heterogeneities, and source radiation pattern. The box indicates a localized region where the velocity structure can be complex[5]. Following a hybrid approach, we compute the velocities and stresses on the leading edge of the box with a generalized ray code assuming a line source. The motions are propagated across this zone containing the ULVZ with the aid of a finite-difference technique. The motions are then interfaced with an analytic code after applying the Kirchkoff method and propagated to the receivers. Detailed comparisons of the output of this hybrid method against analytical methods for plane-layered Earth models demonstrates its accuracy at the various stages of interfacing[5].

Table 1 South American events list

No.	Origin	Latitude (deg)	Longitude (deg)	Depth (km)
1	700604 04:09:25	–9.9	–78.9	57
2	790521 22:22:23	–15.44	–70.04	209
3	700617 4:44:20	–16.0	–71.88	99
4	731025 14:8:58	–21.96	–63.65	517
5	680823 22:36:49	–21.95	–63.64	513
6	671227 8:53:51	–21.2	–68.3	135
7	690725 6:6:42	–25.49	–63.21	573
8	831212 12:21:12	–28.13	–63.15	602
9	670909 10:6:44	–27.62	–63.15	577

Here we analyse recordings of more South American events (Table 1) to further resolve the CMB structure causing the waveform complexity evident in Fig. 2c. These data are displayed in Fig. 3 and grouped according to whether SKS/SPdKS/SKPdS waveform interference is anomalous or normal (PREM-like). The anomalous observations are primarily observed at stations KEV, KRK and KBS, where the separation of SPdKS from SKS develops much earlier than for the normal observations. Complex earthquake rupture characteristics can be ruled out as the cause of the waveform because waveforms at NUR and UME for the same earthquake are relatively simple. Moreover, we infer from this waveform variation at the European stations that SKPdS, but not SPdKS, is the anomalous phase, as the source-side CMB segments for all stations are closely located (Fig. 2a). Additionally, SPdKS waveforms sampling beneath the Americas are normal[8], that is, as displayed in Fig. 2b.

The great-circle paths from the nine events sampling beneath the North Atlantic are displayed in Fig. 4. Again the diffraction paths are indicated by the heavy lines with SKKS and SKS exit points. As SKS and SKKS arrivals fit PREM (Fig. 2c), we can restrict the anomalous region to the area within the heavy contour enclosing the KEV and KRK segments. Henceforth, we will presume that the anomalous waveforms displayed in Fig. 3 are caused by the structure labelled ULVZ (ultra-low-velocity zone).

Considerable progress has been made in modelling anomalous waveforms of the type displayed in Fig. 3 using laterally varying lower-mantle seismic-velocity models[14]. Modelling of SPdKS and SKPdS has been conducted using horizontally stratified velocity layers that are different at the core entry and exit points of the two diffractions. They then arrive at different times, which reduces their overall interference. Fortunately, the branch containing the ULVZ becomes large and occurs earlier in distance. If the ULVZ is at the exit point, the upcoming P wave from the core crosses the zone as P and can be reflected back down to the CMB where it changes mode to S, essentially SKPPS. As the internal reflection at the top of the zone can reach critical angle caused by the velocity increase, the phase SKPPS can be large over a limited distance range, controlled by the ULVZ P-velocity. Increasing this reflection by introducing local sloping structures produces synthetics fitting the KEV records[15]. Thus, we are driven to curve boundaries that can

effectively focus energy downwards, which is one of the reasons for developing the hybrid code discussed in Fig. 1 legend.

After experimenting with a variety of structural shapes (boxcars, domes and triangles), we found that dome shapes produce the types of waveforms typically observed from ULVZs[5]. To sample the model space, we conducted sensitivity tests with various widths, heights and S-velocities. The trade-off of density with S-wave velocity has been discussed previously[8,16]. Structures with widths less than 100 km produce no discernible effects on long-period synthetics, irrespective of their position at the CMB. Broad structures with widths greater than 500 km produce results looking more like the one-dimensional layered synthetics but with reduced SKPPS amplitudes[5]. Dome widths of ~250 km produce the strongest interference with SKS, when the dome is centred on the Pd segment. This shape fits nicely into the contour lines of the ULVZ displayed in Fig. 4 and provides the fortunate set of circumstances allowing this detailed modelling. We selected three sets of synthetics to convey these results (Fig. 3). Synthetics for model 40D are considered to provide the overall best fit as determined by waveform matching (overlay). The 20D model with the reduced shear velocity of 50% fits the top set of records at distances of 106° to 109° the best, but the KBS record (109°) may not be sampling the same structure (see Fig. 4). The recording NUR (105°) is not anomalous but comes from the same event, producing KEV at 106° to demonstrate that the broadness at KEV is not caused by the source. Zones with thicknesses less than 20 km, with large S-wave velocity drops, are particularly good at producing broad pulses. Thicker zones generally produce a stronger SKPdS phase and the prominent waveform distortions. The 80D model with the S-wave velocity drop of 10% produces too much ringing at the larger distances. Thus, our preferred models have greatly reduced shear velocities, indicative of melt.

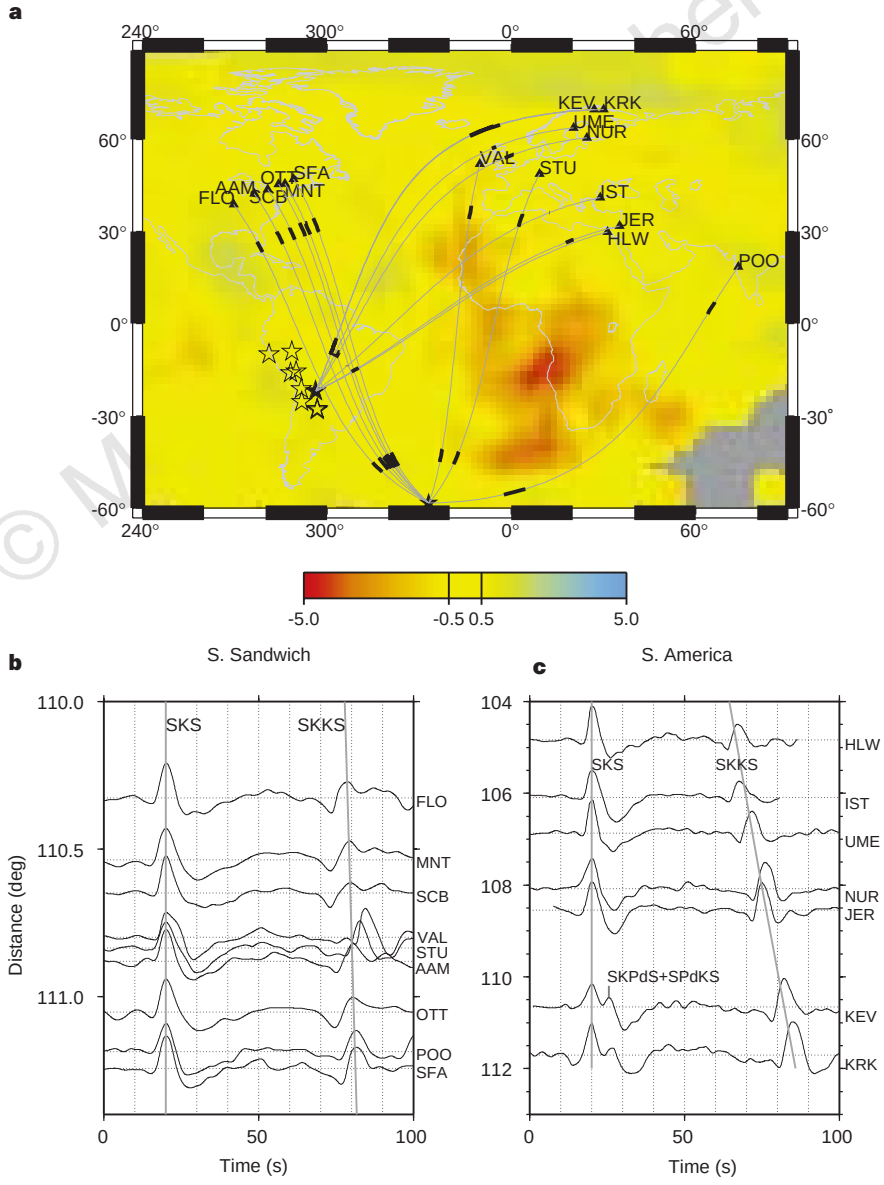

Figure 2 Sampling of the core–mantle boundary and corresponding record section. **a**, Map showing events beneath South Sandwich Island (event 3 in Table 1) and central South America (event 5), along with great-circle paths and heavy line segments indicating the locations of P_{diff} paths (SPdKS and SKPdS) along with the velocity structure of the deep mantle[26]. Colour scale is +5% (blue) to –5% (red). **b**, **c**, Record sections of long-period WWSSN (World Wide Seismographic Station Network) data. The original analogue recordings have been digitized and rotated into SV (radial) and SH (tangential). The SV records have been aligned on the SKS phase and plotted as a function of epicentral distance in degrees. The dotted reference lines are those predicted by PREM indicating normal (SKKS-SKS) differential times and PREM-like lower mantle structures along these paths.

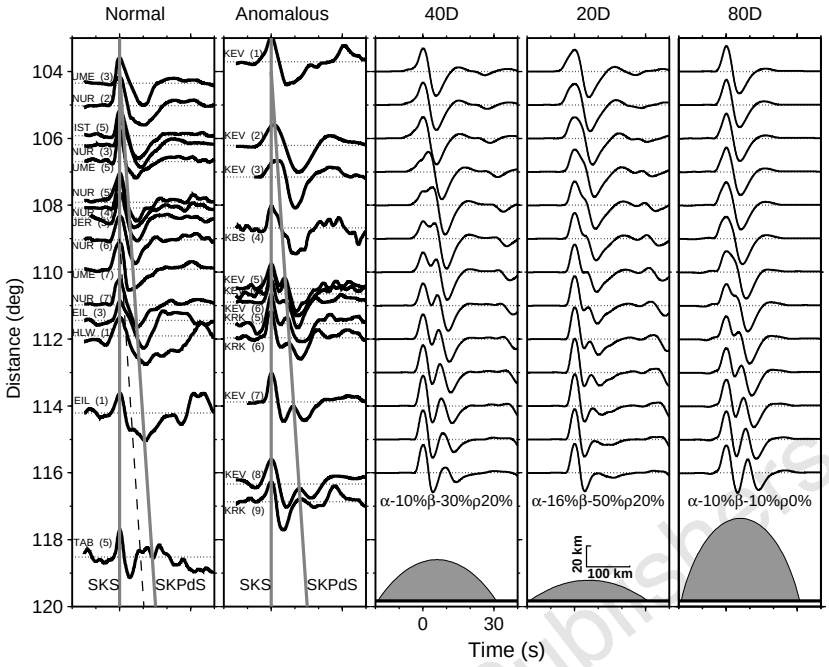

Figure 3 Observations of South American events recorded in Europe divided into two groups, normal and anomalous, along with three sets of synthetics. The observations are aligned on SKS with lines indicating the approximate positions of the diffracted phase SKPdS. The station identification and location are given in Fig. 4 with event indexing keyed to Table 1. We note the complexity of a typical event recorded at KEV relative to NUR. The observations in this record section have been slightly shifted in distance (0.1° change in distance for 50 km change in depth) to correct for the apparent shift in interference pattern[8]. The synthetics were generated from models containing 2D dome structures with a horizontal scale of 250 km located within the patch (ULVZ) in Fig. 4 along the heavy SKPdS line segments. The dome height varies from 20 to 80 km with corresponding S-wave drops of 50 to 10% assuming a 10% drop in P-wave velocity for all models fixed by the apparent position of the interference line (SKPdS). These synthetics were generated with a WKB-type code[13] and contain a WWSSN long-period response, a correction for attenuation $t^* = 1$, and a trapezoidal source function (in seconds) (2,2,2) to be compatible with the observed data[7].

To substantiate our interpretation of this waveform data and to resolve finer detail will require the use of other phases. Core reflections prove very useful for these purposes, as demonstrated for the ULVZ beneath Fiji[17,18] and other ULVZs. Distortions in the precursors to the PKP wavefield also appear useful[19]. These wavefields can be easily added to our hybrid method[20] but prove relatively insensitive to shear velocity variations, as in the case of PcP precursor[17]. Thus the direct seismic evidence presented here for a greatly reduced shear velocity is probably the strongest case for partial melting, which is in agreement with estimates of the reduction of P-to-S velocity ratios based on the physics of molten aggregates[21,22]. Moreover, the relationship of this ULVZ with the upper-mantle thermal anomaly beneath Iceland[23] and the positions of ULVZs and hotspots[24] on a more global scale suggests that these structural features may be related to the "convecting plumes" proposed by the originators of plate-tectonic theory[1]. □

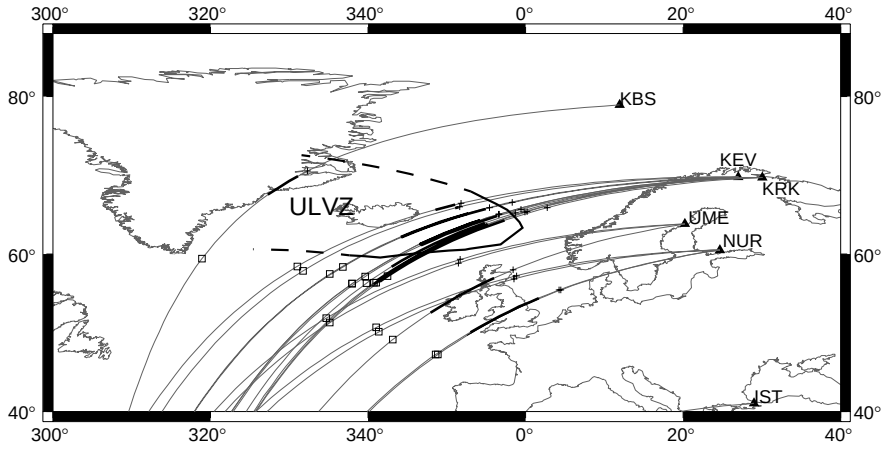

Figure 4 Magnified view of the region beneath the North Atlantic indicating the core-exit points of SKS (crosses) and SKKS (squares). The heavy line segments indicate the diffracted paths along the CMB. The SKPdS segments associated with KEV and KRK appear to be sampling a localized ULVZ located beneath Iceland. D″ velocity structure[26] beneath the North Atlantic is not particularly anomalous, in agreement with the normal travel times of SKS and SKKS at the European stations (Fig. 2c).

Received 4 September 1997; accepted 10 September 1998.

1. Morgan, J. W. Convection plumes in the lower mantle. *Nature* **230,** 42–43 (1971).
2. Olson, P., Schubert, G. & Anderson, C. Plume formation in the D″-layer and the roughness of the core-mantle boundary. *Nature* **327,** 409–413 (1987).
3. Wolfe, C. J., Bjarnason, I. T., VanDecar, J. C. & Solomon, S. C. Seismic structure of the Iceland mantle plume. *Nature* **385,** 245–247 (1997).
4. Nataf, H.-C. & VanDecar, J. C. Seismological detection of a mantle plume? *Nature* **264,** 115–120 (1993).
5. Wen, L. & Helmberger, D. V. A 2D P-SV hybrid method and its applciation to modeling localized structures near the core-mantle boundary. *J. Geophys. Res.* **103,** 17901–17918 (1998).
6. Kind, R. & Müller, G. Computations of SV waves in realistic earth models. *J. Geophys. Res.* **41,** 149–172 (1975).
7. Garnero, E. J., Grand, S. P. & Helmberger, D. V. Low *P*-wave velocity at the base of the mantle. *Geophys. Res. Lett.* **20,** 1843–1846 (1993).
8. Garnero, E. J. & Helmberger, D. V. Seismic detection of a thin laterally varying boundary layer at the base of the mantle beneath the central Pacific. *Geophys. Res. Lett.* **23,** 977–980 (1996).
9. Liu, X.-F. & Dziewonski, A. M. Lowermost mantle shear wave velocity structure (abstr.) *Eos* **75,** 663 (1994).
10. Schweitzer, J. & Müller, G. Anomalous difference travel times and amplitude ratios of SKS and SKKS from Tonga-Fiji events. *Geophys. Res. Lett.* **13,** 1529–1532 (1986).
11. Garnero, E. J. & Helmberger, D. V. A very slow basal layer underlying large-scale low-velocity anomalies in the lower mantle beneath the Pacific: evidence from core phases. *Phys. Earth Planet. Inter.* **91,** 161–176 (1995).
12. Garnero, E. J. & Helmberger, D. V. Further structural constraints and uncertainties of a thin laterally varying ultralow-velocity layer at the base of the mantle. *J. Geophys. Res* **103,** 12495–12509 (1998).
13. Helmberger, D. V., Zhao, L.-S. & Garnero, E. J. in *Seismic Modeling of the Earth Structure* (eds Boschi, E., Ekstrom, G. & Morelli, A.) 183–222 (North-Holland, New York, 1996).
14. Helmberger, D. V., Garnero, E. J. & Ding, X. Modeling two-dimensional structure at the core-mantle boundary. *J. Geophys. Res.* **101,** 13963–13972 (1996).
15. Helmberger, D. V., Wen, L. & Ding, X. Extremes in CMB structure beneath Europe and Africa. *Eos* **78,** 46 (1997).
16. Jeanloz, R. & Garnero, E. J. Interpretation of D″ and the core-mantle boundary region. *Eos* **78,** 46 (1997).
17. Mori, J. & Helmberger, D. V. Localized boundary layer below the mid-Pacific velocity anomaly identified from a P_CP precursor. *J. Geophys. Res.* **100,** 20359–20365 (1995).
18. Revenaugh, J. & Meyer, R. Seismic evidence of partial melt within a possibly ubiquitous low-velocity layer at the base of the mantle. *Science* **277,** 670–673 (1997).
19. Vidale, J. E. & Hedlin, M. A. Intense scattering at the core-mantle boundary north of Tonga: evidence for partial melt. *Nature* **391,** 682–684 (1998).
20. Wen, L. & Helmberger, D. V. Ultra-low velocity zones near the core-mantle boundary from broadband PKP precursors. *Science* **279,** 1701–1703 (1998).
21. Williams, Q. & Garnero, E. J. Seismic evidence for partial melt at the base of Earth's mantle. *Science* **273,** 1528–1530 (1996).
22. Holland, K. G. & Ahrens, T. J. Melting of $(Mg,Fe)_2SiO_4$ at the core-mantle boundary of the Earth. *Science* **275,** 1623–1625 (1997).
23. Shen, Y., Soloman, S., Bjarnason, I. T. & Purdy, G. Hot mantle transition zone beneath Iceland and the adjacent mid-Atlantic Ridge inferred from P-to-S conversions at the 410- and 660-km discontinuities. *Geophys. Res. Lett.* **23,** 3527–3530 (1996).
24. Williams, Q., Revenaugh, J. & Garnero, E. J. A correlation between the hot spot distribution and ultra-low basal velcocities in the mantle. *Science* **281,** 549–564 (1998).
25. Dziewonski, A. M. & Anderson, D. L. Preliminary reference earth model (PREM). *Phys. Earth Planet. Inter.* **25,** 297–356 (1981).
26. Grand, S. P., van der Hilst, R. D. & Widiyantoro, S. Global seismic tomography: A snapshot of convection in the Earth. *GSA Today* **7,** 1–7 (1997).

Acknowledgements. We thank J. Ritsema for comments on early drafts. This work was supported by the NSF.

Correspondence and requests for materials should be addressed to D.V.H. (e-mail: helm@gps.caltech.edu).

Seismic evidence for small-scale dynamics in the lowermost mantle at the root of the Hawaiian hotspot

Sara A. Russell*, Thorne Lay* & Edward J. Garnero†

* *Earth Sciences Department, University of California, Santa Cruz, California 95064, USA*

† *Seismological Laboratory, University of California, Berkeley, California 94720, USA*

The hot thermal boundary layer produced by heat transport from the Earth's core to the base of the mantle is thought to contain strong horizontal shear flows and to nucleate instabilities in which hot material rises into the convecting mantle as thermal plumes[1–3]. A recent study[4,5] proposes that the Hawaiian plume is deflected by mantle convection and, in the lowermost mantle, is located to the southeast of its surface manifestation. Here we present seismic data that densely sample, with core-reflected shear waves, a region beneath the central Pacific Ocean which includes the predicted location of the deflected root of the Hawaiian hotspot. Our mapping of the structure in this region of the lowermost mantle reveals strong lateral gradients in shear-wave velocity and anisotropic shear-wave polarization direction over distances of only several hundred kilometres. We interpret these gradients as being indicative of small-scale dynamical structure in the thermal boundary layer, where vertical flow into the Hawaiian plume at its root is accompanied by horizontal flow towards the plume.

We examine shear waves traversing the deep mantle below a region southeast of Hawaii from 54 earthquakes in the Tonga–Fiji region recorded on 34 digital broadband seismometers in western North America (Fig. 1a). This data set provides better spatial resolution than any other study of deep mantle anisotropy[6] because most previous studies used phases that diffract for long distances along the core–mantle boundary (CMB) and had less dense station distributions.

We analyse shear-wave reflections from the CMB at epicentral distances of 73° to 84° as these provide the best possible spatial sampling of deep mantle structure in our study area. Shallow mantle effects are suppressed by considering ScS differential times relative to the direct S phase (Fig. 1b), which turns at shallower depths in the mantle, and by applying corrections for models of anisotropic lithospheric structure beneath the receivers[7,8]. For the travel-time analysis we use the tangential components of motion (ScSH and SH), as these are free of complexities due to the core-traversing, longitudinally polarized SKS phase in our distance range. The ScS polarization on the tangential and longitudinal (ScSV) components is investigated in the shear-wave splitting analysis.

The central Pacific area studied is known to have anomalous shear-velocity structure in the lowermost mantle. Several global seismic tomography models indicate that our study area has slower-than-average shear velocity, in contrast to faster-than-average velocities characterizing regions beneath margins of the Pacific Ocean[9–12]. A shear-velocity model, M1, with a 3% velocity reduction in the lowermost 200–300 km of the mantle has been proposed for this region[13], and there is compelling evidence for a layer (~10 km thick) above the CMB with strongly reduced velocities (5–10% decreases for P-wave velocity and 15–30% for S-wave velocity)[14–17]. The low shear velocities are likely to indicate hotter than average temperatures, with the very large velocity reductions at the base of the boundary layer suggesting partial melt[18]. Seismic anisotropy, manifested by shear-wave splitting, may result from mineralogical or structural alignments that reflect the strain and/or stress regime in a given region[6,7,19]. Anisotropy with SH faster than SV has been found to the northeast of our study area, and mixed or negligible anisotropy closer to our region[20,21].

Our shear-wave signals are selected to be simple and impulsive to minimize the uncertainties involved in measuring arrival times. Using the cleanest arrival onsets and peaks, we measure differential times between ScSH and SH for a subset of 248 out of 762 seismograms. The differential travel times average 4 s larger than predicted by the reference velocity model PREM[22], much of which can be accounted for by model M1[13]. We find a strong lateral gradient in the differential times anomalies increasing towards the northeast with respect to PREM (Fig. 2a). The ray-path geometry is such that this low-velocity structure need not be strictly confined to the base of the mantle, although absolute travel times indicate that ScS is the phase responsible for the differential behaviour. 3.5% lateral variations in shear velocity in the lowermost 250 km of the mantle over length scales of 600 km can account for the 4 s increase in ScS delay across our study region. Confining the anomalous zone to the lowermost 100 km of the mantle requires extreme lateral gradients of 7% over 300-km scale lengths. Conversely, distributing the anomalous structure over greater depth extent towards the northeast from the CMB reflection points in Fig. 2a allows reduction of